Medical Applications

Snakes and Splines for Tracking Non-Rigid Heart Motion

Amir A. Amini, Rupert W. Curwen, and John C. Gore

333 Cedar St., P.O. Box 208042, Yale University, New Haven, CT 06520
E-mail: amini@minerva.cis.yale.edu

Abstract. MRI is unique in its ability to non-invasively and selectively alter tissue magnetization, and create tagged patterns within a deforming body such as the heart muscle. The resulting patterns (radial or SPAMM patterns) define a time-varying curvilinear coordinate system on the tissue, which we track with B-snakes and coupled B-snake grids. The B-snakes are optimized by a dynamic programming algorithm operating on B-spline control points in discrete pixel space. Coupled B-snake optimization based on an extension of dynamic programming to two dimensions, and gradient descent are proposed. Novel spline warps are also proposed which can warp an area in the plane such that two embedded snake grids obtained from two SPAMM frames are brought into registration, interpolating a dense displacement vector field. The reconstructed vector field adheres to the known displacement information at the intersections, forces corresponding snakes to be warped into one another, and for all other points in the plane, where no information is available, a second order continuous vector field is interpolated.

1 Introduction

In the past, much of the work in image sequence processing has dealt with motion analysis of rigidly moving objects. Non-rigidity however occurs abundantly in motion of both solids and fluids: motion of trees, muscular motion of faces, and non-rigid movement and pumping motion of the left-ventricle (LV) of the heart, as well as fluid motion are all non-rigid [10, 14, 1].

MRI is an excellent imaging technique for measuring non-rigid tissue motion and deformation. MR imaging provides depiction of cardiac anatomy and provides dynamic images with reasonable time resolution that in principle can be used to track the movement of individual segments of myocardium[1] or other structures. In common with other imaging modalities, however, MR images are recorded as selected "snap-shots" at discrete intervals through-out the cardiac cycle that are registered relative to a coordinate system external to the body. Conventional MR or CT imaging therefore can not be used to infer the actual trajectories of individual tissue elements, as such images can only provide geometric information about anatomical object boundaries. Furthermore, since motion of the LV is non-rigid, it is not possible to determine the trajectory of individual

[1] heart muscle

tissue points from boundary information alone, limiting any motion or deformation measurement scheme. To overcome such limitations, tagging methods [19] and phase-contrast [16] measurements of motion have been developed. Phase-contrast techniques provide velocity information about the deforming structure and must be integrated to yield approximate displacements.[2] Tagging techniques allow for direct measurement of displacements at specifically labeled tissue locations.

Leon Axel developed the SPAMM technique in which a striped pattern of altered magnetization is placed within the myocardial tissue [3]. An alternate method described by Zerhouni and co-workers applies a radial array of thin striped tags over a short axis view of the heart [19]. For analysis of tagged images, Prince and his collaborators used optical flow techniques [8], McVeigh et al. used least squares to best localize individual points along a radial tag line assuming known LV boundaries [9], Young and Axel applied FEM models to fit known displacements at tag intersections [18], and Park, Metaxas, and Axel applied volumetric ellipsoids to SPAMM analysis and extracted aspect ratios of their model [15].

Deformable models are powerful tools which can be used for localization as well as tracking of image features [4, 5, 7, 11, 12]. For tagged MR images, several groups have applied snakes for tracking tag lines [2, 18, 17]. In this paper, our efforts are summarized and B-spline snakes in 1D (curves) as well as 2D (grids) are applied to MR tag localization and tracking. A new dynamic programming (DP) algorithm for optimization of B-snakes is proposed. In order to construct an energy field for localization of radial tag lines, we use normalized correlations of simulated image profiles with the data. For SPAMM tags, coupled B-snake grids are used which interact via shared control points. The energy function for coupled B-snake optimization uses the image intensity information along grid lines, as has been used by [2, 18], but sum-of-squared-differences (SSD) of pixel windows at snake intersections are also used in the grid optimization. Optimizing snake grids with standard DP is not possible. For this reason, an extension of DP to two dimensions is discussed where interaction of horizontal and vertical grid lines is allowed. Since this technique is not practical, we have developed a gradient descent algorithm for optimizing spline grids. For SPAMM images, techniques are also discussed for measuring strain as an index of non-rigid deformation from the coupled snake analysis.

Finally, we develop a new class of image warps for bringing two successive snake grids into registration, interpolating a dense displacement vector field. The vector field adheres to the known displacement information at snake intersections, forces corresponding snakes to be warped into one another, and for all other points in the plane, where no information is available, a second order continuous vector field is interpolated.

---

[2] In essence, in the Taylor expansion, $x(t) = x_0 + vt + \frac{1}{2}at^2 + \cdots$, phase-contrast MRI provides v. See [13] for methods for analysis of PC MRI data.

2 Optimization of B-Snakes with Dynamic Programming

B-spline curves are suitable for representing a variety of industrial and anatomical shapes [7, 12, 4, 5]. The advantages of B-spline representations are: (1) They are smooth, continuous parametric curves which can represent open or closed curves. For our application, due to parametric continuity, B-splines will allow for sub-pixel localization of tags, (2) B-splines are completely specified by few control points, and (3) Individual movement of control points will only affect their shape locally. In medical imaging, local tissue deformations can easily be captured by movement of individual control points without affecting static portions of the curve.

2.1 Snake Optimization

To localize each radial tag line, our approach is to minimize the following expression along a quadric B-spline, $\alpha(u)$:

$$E_{total} = -\{\int \rho^n(\alpha(u))du + \rho_e^n(\alpha(0)) + \rho_e^n(\alpha(u_{max}))\} \tag{1}$$

In equation (1), the first term maximizes ρ^n along the length of the snake, and second and third terms attract the snake to the endpoint of tag lines by maximizing ρ_e^n. The limits of summation above include all points on the spline except the two endpoints, $\alpha(0)$ and $\alpha(u_{max})$. Due to the few control points needed to represent tag deformations, we have been able to obtain good results without any additional smoothness constraints on B-splines. In the more general case, the derivative smoothness constraints can also be included.

The discrete form of E_{total}, for a quadric spline may be written as:

$$E_{total} = E_0(p_0, p_1, p_2) + \cdots + E_{N-3}(p_{N-3}, p_{N-2}, p_{N-1}) \tag{2}$$

where p_i is a B-spline control point, and E_i is the sum energy of one B-spline span. DP may be used to optimize the curve in the space of spline control points using the following recurrence

$$S_i(p_i, p_{i+1}) = \min_{p_{i-1}}\{E_{i-1}(p_{i-1}, p_i, p_{i+1}) + S_{i-1}(p_{i-1}, p_i)\} \tag{3}$$

for $i \geq 2$, and $S_1(p_1, p_2) = \min_{p_0} E_0(p_0, p_1, p_2)$. The constructed table, S_i, is called the optimal value function. The window of possible choices for p_{i-1} is typically a 3×3 or a 5×5 pixel area. But, non-square rectangular search areas may be used as well. In general, for an order k B-spline, S_i is a function of k control points, and E_i is a function of $k+1$ control points.[3] Figure 1 shows results from localization and tracking of a cardiac sequence.

[3] Note that the minimization yields the optimal open spline. For other applications, given an external energy field, it may be necessary to optimize a closed snake. In such a case, one performs M applications of the recurrence, where M is the number of possible pixel choices for the endpoint p_i, and for each optimization fixes the *end point* to be one of the M choices, repeating for all M possibilities, and finally choosing the minimum.

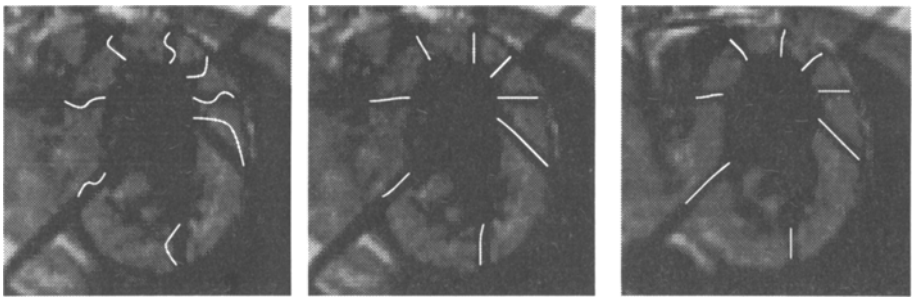

Fig. 1. Results from tracking with B-snakes. Two frames from a sequence are shown. The initial, unoptimized placement of B-snakes is shown on the left. The first image is repeated in the middle, displaying localized tags.

2.2 Snake Energy Field

In a normal MR image, the image intensity is obtained by measuring the NMR signal corresponding to each tissue location. The detected signal is a function of tissue relaxation parameters, as well as the local proton density, and depends on the choice of applied radio-frequency (RF) pulse sequence. In a radial tagged MR image, a series of spatially selective RF pulses is applied prior to a conventional imaging sequence voiding the NMR signal at selective locations, and creating tag patterns within the deforming tissue.

In order to create an external energy field for snake optimization, we simulate time-dependent tag profiles using physics of image formation (see [9]) and concatenate a series of profiles along the vertical axis to create a template (g_1), which subsequently is correlated with the data. Let the image be represented by g_2. The normalized correlation, $\rho(\delta_x, \delta_y)$, between the template g_1 and the image g_2 satisfies $0 \leq \rho \leq 1$, with $\rho = 1$ when g_1 is a constant multiple of g_2. In order to increase the discrimination power of the technique, the energy field is set to $-\rho^n(\delta_x, \delta_y)$, where n is a positive integer less than 10. The higher the value of n, the more discriminating against inexact template matches the energy function becomes, in the limit only *accepting* exact matches. Endpoint energy fields are termed ρ_e, and are obtained from correlating endpoint templates with the tag data.

There is a trade-off between the spatial resolution of this energy field and noise from approximate matches; the degree of trade-off controlled by the template size. The larger the template size, the lower the resolution will be, but the energy field will be more robust to noise and inexact profile matches. The simulated correlation template is successively rotated to create kernels along other orientations. [4]

[4] (0,45,90,135) degrees for 4 radial tag orientations

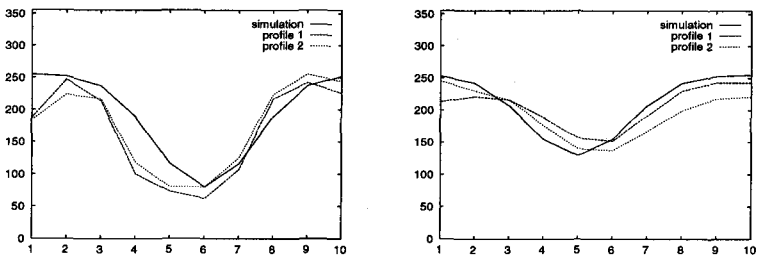

Fig. 2. Comparison of simulated profiles and actual profiles taken from different images.

3 Coupled B-Snake Grids

Coupled snake grids are a sequence of spatially ordered snakes, represented by B-spline curves, which respond to image forces, and track non-rigid tissue deformations from SPAMM data. The spline grids are constructed by having the horizontal and vertical grid lines share control points. By moving a spline control point, the corresponding vertical and horizontal snakes deform. This representation is reasonable since the point of intersection of two tag lines is physically the same material point, and furthermore tissues are connected.

We define a MN spline grid by $(M \times N) - 4$ control points which we represent by the set

$$\{\{p_{12}, p_{13}, \cdots, p_{1,N-1}\}, \{p_{21}, p_{22}, \cdots, p_{2,N}\}, \cdots, \{p_{M,2}, p_{M,3}, \cdots, p_{M,N-1}\}\} \quad (4)$$

where p_{ij} is the spline control point at row i and column j.

3.1 Grid Optimization with Gradient Descent

To detect and localize SPAMM tag lines, we optimize grid locations by finding the minimum intensity points in the image, as tag lines are darker than surrounding tissues. However, there is an additional energy term present in our formulation which takes account of the local 2D structure of image intensity values at tag intersections. Although we can not specify an exact correspondence for points along a tag line, we do know the exact correspondence for points at tag intersections. This is the familiar statement of aperture problem in image sequence analysis. The way to incorporate this familiar knowledge into our algorithm is by use of the SSD function in (5). The energy function which we minimize is

$$\mathcal{E}(p_{12}, \cdots, p_{M,N-1}) = \lambda_1 \sum_k \int I(\alpha_k(u))du + \lambda_2 \sum_{ij} SSD(v_{ij}) \quad (5)$$

where v_{ij} denotes the intersection point of horizontal and vertical snake curves, and λ_1 and λ_2 are pre-set constants. The SSD function determines the sum-of-squared-differences of pixels in a window around point v_{ij} in the current frame

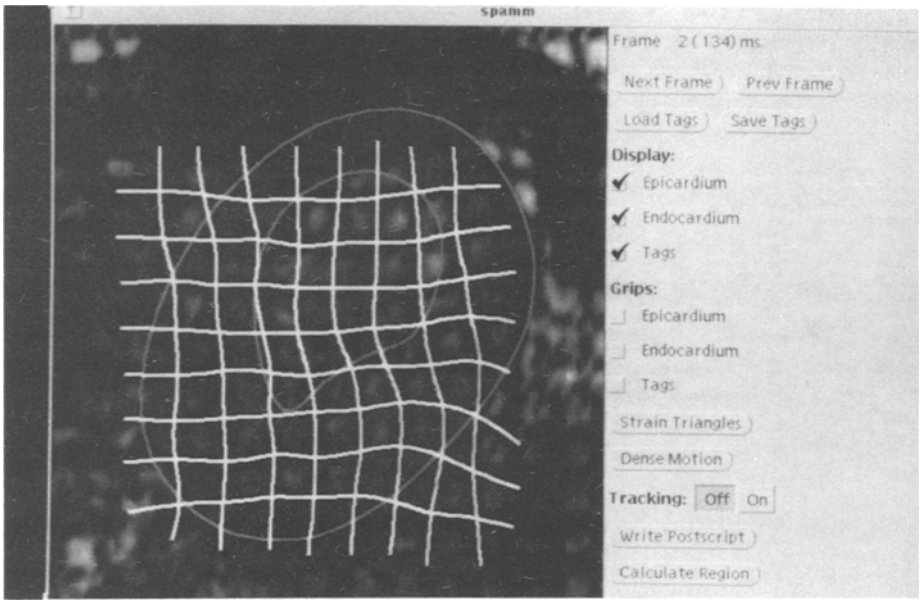

Fig. 3. Locating tag lines in SPAMM images. An intermediate frame in a sequence of tagged images is shown. The LV contours in the figure are hand-drawn B-spline curves. Note that the portions of the snake grids lying within the ventricular blood and in the liver do not contribute to the energy of the snake grid.

with a window around the corresponding B-snake grid intersection in the next frame. In order to minimize the discretized version of $\mathcal{E}$, in each iterative step, we compute the gradient of $\mathcal{E}$ with respect to p_{ij}, perform a line search in the $\bigtriangledown\mathcal{E}$ direction, move the control points to the minimum location, and continue the procedure until the change in energy is less than a small number, defining convergence. In practice, we have an additional constraint in computing the energy function: we only use the intersections, and points on the snake grid which lie on the heart tissue. Results from grid optimization for localization and tracking of a spline grid with gradient descent is shown in figure 3.

3.2 Grid Optimization with Dynamic Programming

In this section, we describe a DP formulation for grid optimization. We note that optimizing an interacting grid with standard DP is not possible due to the dependence of horizontal and vertical snakes on one another.

As stated in section 2, the DP optimal value function for 1D splines is a function of spline control points. To apply 2D DP to this problem, we define the optimal value function, $S : \mathcal{R} \times \mathcal{F} \longrightarrow \mathcal{R}$ with $\mathcal{R}$ denoting the real line and $\mathcal{F}$ being a space of one dimensional splines

$$S(x, V_k(x,.)) = \min_j \{S(x + \Delta x, V_j(x + \Delta x,.)) + \mathcal{E}_1(V_k(x,.), V_j(x + \Delta x,.)) + \mathcal{E}_2(V_j(x + \Delta x,.))\} \quad (6)$$

where x is a real number indexing location along the horizontal axis of the image where tag lines are located. Δx represents vertical tag separation, and V represents a realization of a spline. The class of all admissible vertical splines is $\mathcal{F}$. Note that

$$\mathcal{E}_1(V_j(x+\Delta x,.),V_k(x,.)) = \sum_i \int -I(H_i(u))du \tag{7}$$

where i indexes horizontal snakes between x and $x+\Delta x$, H_i is snake number i, and $1 \leq i \leq m$ with m being the number of horizontal snakes. $\mathcal{E}_2(V_j(x+\Delta x,.))$ is the energy of spline number j at location $x+\Delta x$

$$\mathcal{E}_2(V_j(x+\Delta x,.)) = -\int I(V_j(x+\Delta x,u))du \tag{8}$$

We have defined a recursive form for obtaining optimal grids with the new DP algorithm. Finally, we note that this algorithm is not practical, since we need to know all the possible deformations of a vertical or horizontal snake before hand. Moreover, the stated formulation will only apply to linear splines (to further generalize to non-linear splines, $\mathcal{E}_1$ will depend not only on splines at x and $x+\Delta x$, but also on other neighboring splines). On the positive side, if all the possible deformations were known, the 2D DP algorithm would guarantee the global optimality of the grid.

3.3 Tissue Strain from Snake Interactions

Strain is a measure of local deformation of a line element due to tissue motion and is independent of the rigid motion. To compute the local 2D strain for a given triangle, correspondence of 3 vertices with a later time is sufficient. With this information known, an affine map F is completely determined. Under the local affine motion assumption for the LV, strain in the direction of vector $\mathbf{x}$ can be expressed as

$$\Sigma = \frac{1}{2}\left(\frac{|F\mathbf{x}|^2}{\mathbf{x}^T\mathbf{x}} - 1\right) \tag{9}$$

Two directions within each such triangle are of particular interest, namely, the directions of principal strain, representing the maximum and minimum stretch within a triangle. The results of strain analysis performed on a typical tagged image is shown in figure 4 with the corresponding maximum and minimum principal strain directions and values.

4 Smooth Warps

Tracking tissue deformations with SPAMM using snake grids provides 2D displacement information at tag intersections and 1D displacement information along other 1D snake points. In this section, we describe *smooth warps* which

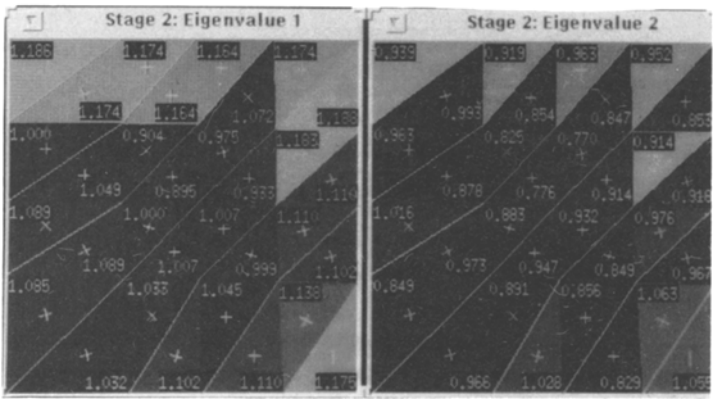

Fig. 4. Strain measurement made from two SPAMM frames.

reconstruct a dense displacement vector field using the optimized snakes and the available displacement information, assuming only 2D motion (as is roughly the case towards the apical end of the heart). We note that this analysis can be extended to 3D.

To proceed more formally, the continuity constraint is the bending energy of a thin-plate which is applied to the x and y component of the displacement field $(u(x,y), v(x,y))$:

$$\int\int u_{xx}^2 + 2u_{xy}^2 + u_{yy}^2 dxdy \tag{10}$$

$$\int\int v_{xx}^2 + 2v_{xy}^2 + v_{yy}^2 dxdy \tag{11}$$

These constraints serve as the smoothness constraints on the reconstructed vector field, characterizing approximating thin-plate splines [6].

With the intersection springs in place,

$$\sum (u - d^u)^2 + (v - d^v)^2 \tag{12}$$

is also to be minimized. In (12), d^u and d^v are the x and y components of displacement at tag intersections. The form of the intersection spring constraints is similar to depth constraints in surface reconstruction from stereo, and has also been used in a similar spirit by Young et al. [18].

Assuming 2D tissue motion, a further physical constraint is necessary: any point on a snake in one frame must be displaced to lie on its corresponding snake in all subsequent frames. This constraint is enforced by introducing a sliding spring. One endpoint of the spring is fixed on a grid line in the first

frame, and its other endpoint is allowed to slide along the corresponding snake in the second frame, as a function of iterations. We minimize

$$\sum \{(x+u-\bar{x})^2 + (y+v-\bar{y})^2\} \tag{13}$$

along 1D snake points. In the above equation, (x, y) are the coordinates of a point on the snake in the current frame, and $(\bar{x}, \bar{y})$ is the closest point to $(x+u, y+v)$ on the corresponding snake in the second frame. Adding (10), (11), (12), and (13), and deriving the Euler-Lagrange equations will yield a pair of equations involving partial derivatives of $(\bar{x}, \bar{y})$: [5]

$$\begin{aligned}
\lambda_1 \nabla^4 u + \lambda_2(u-d^u) + \lambda_3 \{(u+x-\bar{x})(1-\bar{x}_u) + (v+y-\bar{y})(-\bar{y}_u)\} = 0 \\
\lambda_1 \nabla^4 v + \lambda_2(v-d^v) + \lambda_3 \{(v+y-\bar{y})(1-\bar{y}_v) + (u+x-\bar{x})(-\bar{x}_v)\} = 0
\end{aligned} \tag{14}$$

where $\lambda_1 \geq 0$ everywhere, $\lambda_2 \geq 0$ at tag intersections, and $\lambda_3 \geq 0$ at all 1D snake points. We now make two approximations. For vertical grids, the x-coordinates of curves only vary slightly, and as the grid lines are spatially continuous, $\bar{x}_u$ is expected to be small. Furthermore, for vertical grids $\bar{y}$ changes minutely as a function of u, so that $\bar{y}_u \approx 0$. For horizontal grids, the y coordinates of curves also vary slightly along the length of grid lines, and since these are spatially continuous curves, $\bar{y}_u$ is expected to be small. Note that these approximations will hold under smooth local deformations, as is expected in the myocardial tissue. Only $\bar{x}_u$ for horizontal grids, and $\bar{y}_v$ for vertical grids is expected to vary more significantly. Though the effect of these terms is to modulate λ_3, for completeness, we include these derivatives in our equations:

$$\begin{aligned}
\lambda_1 \nabla^4 u + \lambda_2(u-d^u) + \lambda_3(u+x-\bar{x})(1-T_{hor}\bar{x}_u) = 0 \\
\lambda_1 \nabla^4 v + \lambda_2(v-d^v) + \lambda_3(v+y-\bar{y})(1-T_{ver}\bar{y}_v) = 0
\end{aligned} \tag{15}$$

The variables T_{hor} and T_{ver} are predicates equal to one if the snake point of interest lies on a horizontal, or a vertical grid line. An iterative solution to (15) from finite differences has been adopted which converges in 400-500 iterations for two SPAMM frames.

The results of applying (15) to two snake grids in figure 7 is shown in figure 5 with $\lambda_1 = 8.0$, $\lambda_2 = 1.0$, and $\lambda_3 = 10.0$. At iteration 1, $NZP = 1008$, $TPS = 12429.06$, $IE = 432.06$, and $PE = 2742.26$. At convergence, $NZP = 298$, $TPS = 68.52$, $IE = 1.39$, and $PE = 56.22$. Where IE is given by equation (12) , and PE is given by equation (13). NZP is the number of non-zero points in a 2D scratch array where all snake coordinates on both snake grids are exclusive-ored together. The thin-plate spline measure (TPS) is the sum of the two integral measures in equations (10), and (11). These measures were computed for (intersection and grid) points within the myocardium. Note that PE does not include the intersection points.

Utilizing the dense displacement vector field recovered with the method outlined in this section, in addition to strain, differential measures describing local

[5] Note that in practice, $(\bar{x}, \bar{y})$ is smoothed by local averaging

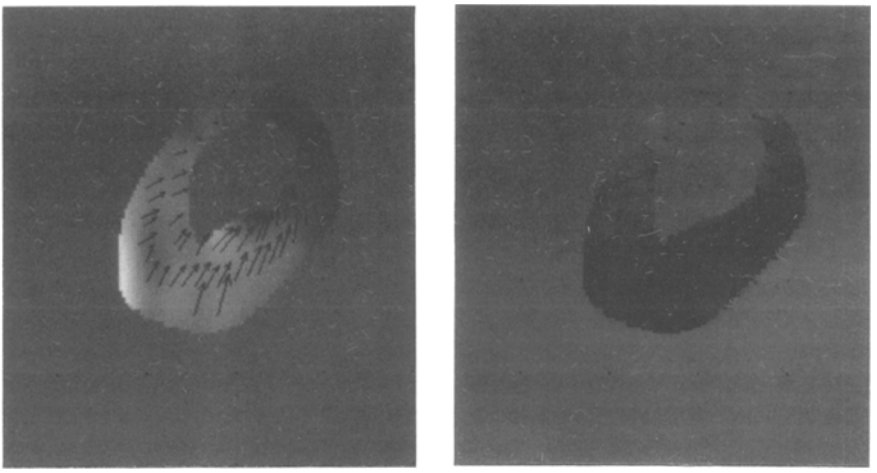

Fig. 5. Reconstruction of dense u and v components of displacement from 2 snake grids in figure 3. The vector field is superimposed on the u, and v reconstructions for the final results (iteration 500).

rotations and expansions may be obtained. Tissue expansion or contraction in an arbitrary area may be computed by applying Gauss's theorem, and local tissue rotations may be computed by applying Stoke's theorem. As a final note, the dense displacement field suggested here can only be an approximation to the true displacement vector field. However, as the tag lines become closer, the approximation becomes very accurate.

5 Conclusions

In conclusion, we have described new computational algorithms suitable for analysis of both radial and SPAMM tagged data. We described a new DP algorithm which given an external energy field, can optimize B-snakes. We have argued that in comparison to other forms of parametrization, use of B-splines for representing curves has several advantages, including subpixel accuracy for tag localization and parametric continuity, as well as the need to only optimize the location of few control points in order to determine the location of a complete tag line.

A different aspect of our work involves reconstruction and interpolation of dense displacement vector fields directly from tracked snake grids. To this end, we presented smooth warps which warp an area in the plane such that two embedded grids of curves are brought into registration.

References

1. A. A. Amini. A scalar function formulation for optical flow. In *European Conference on Computer Vision*, Stockholm, Sweden, May 1994.
2. A. A. Amini and et al. Energy-minimizing deformable grids for tracking tagged MR cardiac images. In *Computers in Cardiology*, pages 651–654, 1992.
3. L. Axel, R. Goncalves, and D. Bloomgarden. Regional heart wall motion: Two-dimensional analysis and functional imaging with MR imaging. *Radiology*, 183:745–750, 1992.
4. B. Bascle and R. Deriche. Stereo matching, reconstruction, and refinement of 3d curves using deformable contours. In *International Conference on Computer Vision*, 1993.
5. A. Blake, R. Curwen, and A. Zisserman. A framework for spatio-temporal control in the tracking of visual contours. *International Journal of Computer Vision*, 11(2):127–145, 1993.
6. F. Bookstein. Principal warps: Thin-plate splines and the decomposition of deformations. *IEEE Transactions on PAMI*, 1989.
7. A. Gueziec. Surface representation with deformable splines: Using decoupled variables. *IEEE Computational Science and Engineering*, pages 69–80, Spring 1995.
8. S. Gupta and J. Prince. On variable brightness optical flow for tagged MRI. In *Information Processing in Medical Imaging (IPMI)*, pages 323–334, 1995.
9. M. Guttman, J. Prince, and E. McVeigh. Tag and contour detection in tagged MR images of the left ventricle. *IEEE-TMI*, 13(1):74–88, 1994.
10. T. Huang. Modeling, analysis, and visualization of nonrigid object motion. In *International Conference on Pattern Recognition*, 1990.
11. M. Kass, A. Witkin, and D. Terzopoulos. Snakes: Active contour models. *International Journal of Computer Vision*, 1(4):321–331, 1988.
12. S. Menet, P. Saint-Marc, and G. Medioni. B-snakes: Implementation and application to stereo. In *International Conference on Computer Vision*, pages 720–726, 1990.
13. F. Meyer, T. Constable, A. Sinusas, and J. Duncan. Tracking myocardial deformations using spatially constrained velocities. In *IPMI*, pages 177–188, 1995.
14. C. Nastar and N. Ayache. Non-rigid motion analysis in medical images: A physically based approach. In *IPMI*, pages 17–32, 1993.
15. J. Park, D. Metaxas, and L. Axel. Volumetric deformable models with parameter functions: A new approach to the 3d motion analysis of the LV from MRI-SPAMM. In *International Conference on Computer Vision*, pages 700–705, 1995.
16. N. Pelc, R. Herfkens, A. Shimakawa, and D. Enzmann. Phase contrast cine magnetic resonance imaging. *Magnetic Resonance Quarterly*, 7(4):229–254, 1991.
17. D. Reynard, A. Blake, A. Azzawi, P. Styles, and G. Radda. Computer tracking of tagged 1H MR images for motion analysis. In *Proc. of CVRMed*, 1995.
18. A. Young, D. Kraitchman, and L. Axel. Deformable models for tagged MR images: Reconstruction of two- and three-dimensional heart wall motion. In *IEEE Workshop on Biomedical Image Analysis*, pages 317–323, Seattle, WA, June 1994.
19. E. Zerhouni, D. Parish, W. Rogers, A. Yang, and E. Shapiro. Human heart: Tagging with MR imaging – a method for noninvasive assessment of myocardial motion. *Radiology*, 169:59–63, 1988.